Crossed-Beams and Theoretical Studies of the $O(^3P) + H_2O \rightarrow HO_2 + H$ Reaction Excitation Function

Amy L. Brunsvold, Jianming Zhang, Hari P. Upadhyaya, and Timothy K. Minton*

Department of Chemistry and Biochemistry, Bozeman, Montana 59717

Jon P. Camden, Jeffrey T. Paci, and George C. Schatz*

Department of Chemistry, Northwestern University, Evanston, Illinois 60208

Received: June 7, 2007; In Final Form: August 8, 2007

Ⓦ **This paper contains enhanced objects available on the Internet at http://pubs.acs.org/jpca.**

Hyperthermal collisions of ground-state atomic oxygen with H_2O have been investigated, with special attention paid to the H-atom elimination reaction, $O(^3P) + H_2O(X\ ^1A_1) \rightarrow HO_2(^2A') + H(^2S)$. This reaction was observed in a crossed-beams experiment, and the relative excitation function in the region around its energy threshold (50−80 kcal mol^{-1}) was measured. Direct dynamics calculations were also performed at two levels of theory, B3LYP/6-31G(d,p) and MP2/6-31G(d,p). The shape of the B3LYP excitation function closely matches that of the experiment. The calculations provided a detailed description of the dynamics and revealed a striking dependence of the reaction mechanism on collision energy, where the cross section rises from a threshold near 60 kcal mol^{-1} to a peak at ∼115 kcal mol^{-1} and then decreases at higher energies as secondary dissociation of the internally excited HO_2 product becomes dominant. The calculations show that the cross section for H-atom elimination ($O + H_2O \rightarrow HO_2 + H$) is about 10−25% that of the H-atom abstraction ($O + H_2O \rightarrow OH + OH$) cross section for collision energies in the 70−160 kcal mol^{-1} range.

I. Introduction

Hyperthermal interactions of $O(^3P)$ with $H_2O(X^1A_1)$ occur in the vicinity of space vehicles that travel through the Earth's residual atmosphere at altitudes higher than ∼100 km.[1−10] H_2O is a major outgassing product from space vehicles and may also be released from manned spacecraft during wastewater dumps. It is a major component of rocket exhaust gas and, therefore, may exit maneuvering engines and other propulsion systems at velocities that exceed 3000 m s^{-1}. $O(^3P)$ atoms dominate the residual atmosphere of the Earth at altitudes from approximately 150 to 700 km. Thus, because space vehicles travel at orbital or suborbital velocities approaching 8 km s^{-1}, ambient $O(^3P)$ atoms collide with expelled H_2O molecules at high relative velocities. For example, a relative velocity of 8 km s^{-1} corresponds to $O(^3P) + H_2O$ collisions with a center-of-mass (c.m.) collision energy of 64.8 kcal mol^{-1}. High-energy collisions between $O(^3P)$ and H_2O may give rise to infrared (IR) radiation resulting from internally excited products, and if the collision energy is sufficiently high, ultraviolet (UV) emission may be observed from electronically excited products, such as $OH(A^2\Sigma^+)$. The importance of IR and UV emission from hyperthermal $O(^3P) + H_2O$ collisions in the vicinity of space vehicles has motivated a number of space-based and laboratory experiments, as well as theoretical studies of the inelastic and reactive pathways. The work to date has focused on three pathways: $O(^3P) + H_2O[X^1A_1(\nu_1\nu_2\nu_3,JK)] \rightarrow O(^3P) + H_2O[X^1A_1(\nu_1'\nu_2'\nu_3',J'K')]$,[4,5,7,11] $OH(X^2\Pi) + OH(X^2\Pi)$,[7,10−13] and $OH(A^2\Sigma^+) + OH(X^2\Pi)$.[9,14] Additional pathways on the H_2O_2 triplet potential energy surfaces have also been considered.[15]

An energy diagram showing potential products of $O(^3P)$ reactions with H_2O is shown in Figure 1. H-atom abstraction,

$$O(^3P) + H_2O(X^1A_1) \rightarrow OH(X^2\Pi) + OH(X^2\Pi) \quad (1)$$

is the reactive channel with the lowest barrier, but at collision energies greater than ∼60 kcal mol^{-1}, two additional primary channels become accessible: a molecular channel that forms $H_2(^1\Sigma_g^+) + O_2(^3\Sigma_g^-)$[15] and an H-atom elimination channel,

$$O(^3P) + H_2O(X^1A_1) \rightarrow HO_2(^2A') + H(^2S) \quad (2)$$

The transition-state structures and energies for reactions 1 and 2 are shown in Figure 1. The $H_2 + O_2$ product valley is not accessible from the $O + H_2O$ reactant valley through a transition state with a single imaginary frequency.[15] $H_2 + O_2$ can be formed through a transition state that connects to $HO_2 + H$, but we find that $H_2 + O_2$ is not formed directly from collisions between O and H_2O, even at energies sufficiently high to produce $HO_2 + H$.[16] At collision energies greater than 100 kcal mol^{-1} (such as those that might occur when a rocket engine is fired in the same direction in which the spacecraft is traveling—i.e., the ram direction), fragmentation into three bodies or electronic excitation of OH become energetically allowed (see Figure 1).

H-atom elimination was observed in studies of hyperthermal O-atom reactions with CH_4[17] and HCl,[18] yet the importance of analogous elimination reactions was not investigated in earlier studies of $O + H_2O$ collisions. In addition, there are no reports of $O(^3P) + H_2O$ reactions producing $HO_2 + H$, presumably because of the large reaction endoergicity.

* Corresponding authors. E-mail: T.K.M., tminton@montana.edu; G.C.S., schatz@chem.northwestern.edu.

10.1021/jp0744228 CCC: $37.00
Published on Web 10/10/2007

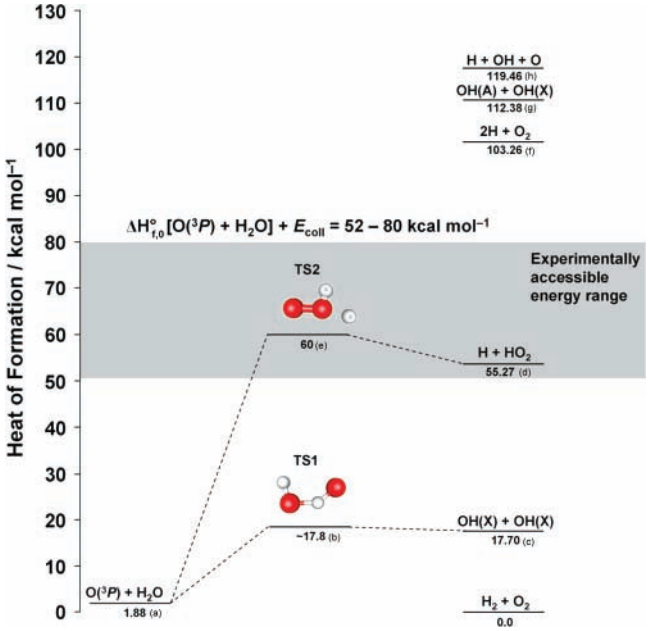

Figure 1. Enthalpy diagram for various products of the $O(^3P) + H_2O$ reaction. The shaded horizontal band shows the enthalpy range that was accessible in the experiment by varying the collision energy. Thermochemical data were derived from (a) refs 39 and 40, (b) refs 10 and 41, (c) ref 40, (d) ref 42, (e) current work, (f) ref 39, (g) ref 9, and (h) refs 39 and 40.

Here we report the results of experimental and theoretical studies of hyperthermal collisions of $O(^3P) + H_2O(X^1A_1)$, with special attention paid to the H-atom elimination reaction. We observed this reaction in a crossed-beams experiment, and we measured the relative excitation function in the region of the energy threshold (50−80 kcal mol^{-1}; see Figure 1). Using Born−Oppenheimer molecular dynamics at the B3LYP/6-31G(d,p) level of theory, the excitation function was calculated. The transition states of reactions 1 and 2 were characterized with the use of *ab initio* electronic structure calculations. These calculations provide detailed insight into aspects of $O(^3P) + H_2O$ collision dynamics that are not accessible in the experiment.

II. Theoretical Methods

A. Stationary Point Characterization. An extensive search for stationary points on the lowest triplet H_2O_2 potential energy surface (PES) was previously conducted by Karkach and Osherov.[15] The main transition states connecting the $O + H_2O$, $HO_2 + H$, $OH + OH$, and $H_2 + O_2$ valleys of the PES were identified and optimized at the QCISD(T)/6-311(d,p) level of theory. All of the structures were found to be planar, and only two of them connect to the $O + H_2O$ reactant valley. We note that the lowest H_2O_2 triplet state in C_s symmetry is $^3A''$. In the present work, we refer to the lowest saddle points leading from the $O + H_2O$ reagent valley to the $OH + OH$ and $HO_2 + H$ product valleys as transition state 1 (TS1) and transition state 2 (TS2), respectively.

Although the characterization of TS1 has been the subject of several earlier investigations,[15,19,20] TS2 has received very little attention. Therefore, we seek to characterize TS1 and TS2 on the lowest triplet PES at a high level of theory and to explore lower-level electronic structure methods that are computationally tractable for direct dynamics simulations. Calculations of the saddle points were performed with Q-Chem version 2.1[21] and MOLPRO[22] electronic structure codes. Coupled-cluster calculations with singles, doubles, and perturbative triples [CCSD(T)],[20,23] employing the aug-cc-pVTZ basis, represent the highest level of theory employed in this work.

Reaction energies, barrier heights, and saddle point geometries for calculations at the MP2/6-31G(d,p), B3LYP/6-31G(d,p), CCSD/cc-pVTZ, and CCSD(T)/aug-cc-pVTZ levels of theory are compared with experimental values in Table 1. All calculations except for the CCSD(T)/aug-cc-pVTZ calculations performed in MOLPRO employed unrestricted Hartree−Fock reference wavefunctions. We also explored MP2/cc-pVTZ calculations; however, little improvement from the MP2/6-31G(d,p) energies was observed. As the reaction barriers are critical for obtaining accurate excitation functions, we focus our discussion on the saddle point properties. The geometries obtained for TS1 at the MP2, CCSD, and CCSD(T) levels are in reasonable agreement. We were not able to confirm the existence of a transition state connecting $O + H_2O$ and $OH +$

TABLE 1: Energetics and Transition-State Properties for the Various Reaction Pathways on the Lowest Triplet H_2O_2 Potential Energy Surface[a]

	B3LYP/6-31G(d,p)	MP2/6-31G(d,p)	CCSD/cc-pVTZ	CCSD(T)/aug-cc-pVTZ	expt[b]
		$O + H_2O \rightarrow TS1 \rightarrow OH + OH$			
ΔE	14.6 (11.8)	22.4 (19.7)	19.1 (16.2)	18.9 (16.1)	(15.82)
$\Delta E^{\ddagger}$		28.4 (25.1)	24.3 (20.8)	21.2 (18.0)	
r_1		0.97	0.97	0.97	
r_2		1.24	1.23	1.26	
r_3		1.08	1.10	1.09	
θ_1		105.4	104.4	106.3	
θ_2		142.9	145.4	141.1	
		$O + H_2O \rightarrow TS2 \rightarrow HO_2 + H$			
ΔE	47.7 (43.1)	58.5 (53.9)	62.8 (58.3)	59.4 (54.8)	(53.39)
$\Delta E^{\ddagger}$	59.6 (56.2)	87.2 (84.3)	80.2 (76.7)	74.3 (70.9)	(60 ± 2)
r_1	1.48	1.46	1.50	1.50	
r_2	0.98	0.97	0.97	0.97	
r_3	1.46	1.35	1.45	1.46	
θ_1	101.5	101.3	99.6	100.0	
θ_2	96.4	95.2	93.7	94.3	
		$O + H_2O \rightarrow O_2 + H + H$			
ΔE	100.2 (89.1)	96.4 (84.7)	115.9 (104.7)	113.3 (102.1)	(101.38)
		$O + H_2O \rightarrow OH + H + O$			
ΔE	119.7 (111.7)	118.9 (110.7)	120.6 (112.3)	123.6 (115.5)	(117.58)

[a] Distances in angstroms; energies in kcal mol^{-1}. Zero-point-corrected values are given in parentheses. TS1 distances: $r_1 = r$(H1−O1), $r_2 = r$(O1−H2), $r_3 = r$(H2−O2), $\theta_1 = \angle$(H1−O1−H2), $\theta_2 = \angle$(O1−H2−O2). TS2 distances: $r_1 = r$(O1−O2), $r_2 = r$(O2−H1), $r_3 = r$(O2−H2), $\theta_1 = \angle$(O1−O2−H1), $\theta_2 = \angle$(H1−O2−H2). [b] Derived from enthalpies of formation at 0 K: see Figure 1.

OH at the B3LYP level of theory. This is likely due to the fact the B3LYP often underestimates reaction barriers,[24−26] and TS1 is very close in energy to the OH + OH product valley. As expected, the barrier height to reaction 1 decreases as higher levels of electron correlation are included in the calculations. At the CCSD(T) level of theory, the zero-point-corrected barrier for reaction 1 is 17.7 kcal mol^{-1} above $O + H_2O$ and 1.6 kcal mol^{-1} above OH + OH.

The TS2 geometries obtained at the B3LYP, CCSD, and CCSD(T) levels are in good agreement, and TS2 is product-like, which is expected for a highly endothermic reaction. Similar to the trend observed in reaction 1, the barrier height for reaction 2 decreases upon inclusion of higher levels of electron correlation. However, even the CCSD(T) calculations predict a barrier more than 10 kcal mol^{-1} higher than the experimentally determined threshold (*vide infra*) of 60 ± 2 kcal mol^{-1}. Examination of the calculations based on unrestricted wavefunctions (MP2 and CCSD) indicate that the reference wavefunction exhibits significant spin contamination ($\langle S^2 \rangle \sim 2.2$), which suggests that this region of the PES is multireference in character. In fact, of the methods examined, the B3LYP barrier height is the closest to the experiment, being only ∼4 kcal mol^{-1} too low. Therefore, of the computationally tractable methods for direct dynamics calculations, i.e., B3LYP/6-31G-(d,p) and MP2/6-31G(d,p), we find that B3LYP provides the best comparison with the experimentally determined reaction energetics and barrier heights. Indeed, as will be shown, our direct dynamics calculations on B3LYP are in much better agreement than those on MP2.

B. Details of the Quasiclassical Trajectory Calculations. Batches of 500−900 quasiclassical trajectory calculations were run at a variety of collision energies (E_{coll}) between 64.6 and 161 kcal mol^{-1} to calculate reaction cross sections for the OH + OH (σ_{OH}), HO_2 + H (σ_{HO_2}), and fragmentation (σ_{frag}) product channels. Trajectories were integrated using a standard fifth-order predictor, sixth-order corrector integration algorithm.[27,28] At each point along the trajectory, the energy and gradient were obtained from either a B3LYP/6-31G(d,p) or MP2/6-31G(d,p) calculation in Q-Chem. The initial conditions were sampled randomly over initial orientations and impact parameter. A single intramolecular trajectory starting from the equilibrium H_2O geometry was run with kinetic energy corresponding to the zero-point energy in each normal mode. The H_2O vibrational phase for each reactive trajectory was then sampled randomly from the initial intramolecular trajectory. The maximum impact parameter (b_{max}) was either 4.8 or 5.0 au. In each batch of trajectories, our choice of b_{max} was justified by examination of the opacity function. The integration time step was held constant at 10.0 au for all trajectories. Energy conservation was required to be better than 3 kcal mol^{-1} in total energy, and spin-contamination was checked at each time step during trajectory propagation. Less than 0.1% of the trajectories violate energy conservation, and these violations were attributed to problems in convergence of the self-consistent field (SCF) calculation (i.e., the SCF failed to converge or converged to the wrong electronic state during trajectory propagation) and not the integration time step. For the higher energies, larger values of spin contamination are observed for trajectories that lead to fragmentation, which is expected as several bonds are broken. We retain these trajectories, however, because their neglect would lead to inaccurate fragmentation cross sections. Integration was terminated when the distance between any two atoms exceeded 10 au. We did not discard product trajectories with an internal energy below the harmonic zero point, as this can lead to an underestimation of the cross section.[29−31] When fragmentation occurs, the light H atom can often move beyond the 10 au limit before HO_2 can dissociate. In these cases, we calculated the internal energy of the HO_2 product, and if it exceeded the threshold for fragmentation into H + H + O_2, we assigned that trajectory to fragmentation. Note that our calculations do not distinguish between the H + H + O_2 and H + OH + O channels.

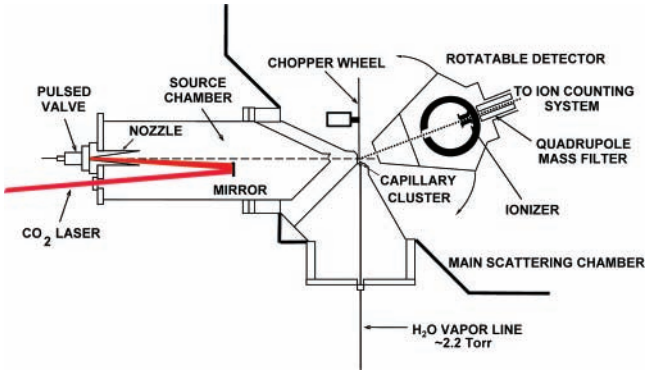

Figure 2. Schematic diagram of the crossed molecular beams apparatus, including laser detonation source, rotatable mass spectrometer detector, and effusive water source with capillary cluster.

III. Experimental Methods

The experiments were performed with a crossed-molecular beams apparatus and hyperthermal atomic-oxygen beam source that are described elsewhere.[32−34] Figure 2 shows a schematic diagram of the apparatus configured for crossed-beams studies of $O + H_2O$ collisions. A pulsed hyperthermal beam containing ∼90% $O(^3P)$ and ∼10% $O_2(^3\Sigma_g^-)$ was produced by laser heating.[35,36] This beam passed through two regions of differential pumping and entered the main scattering chamber, where it crossed a continuous beam of H_2O molecules. Products that scattered from the crossing region were detected with a rotatable mass spectrometer detector. To prepare hyperthermal O-atom beams with relatively narrow and variable velocity distributions, a synchronized chopper wheel was used to select a portion of the overall hyperthermal pulse. The nominal velocity of the O-atom beam was varied by adjusting the synchronization between a photodiode on the chopper wheel and the initiation of the hyperthermal pulse. The chopper was 17.8 cm in diameter and rotated at 300 Hz. It had three equally spaced slots, each 1.5 mm wide, and it was placed about 97 cm from the apex of the conical nozzle and 2 cm from the axis of the H_2O beam. The mass spectrometer detector was used to monitor the hyperthermal O-atom beam, and the velocity distributions in the O-atom beam pulses were determined by the time-of-flight method.

The main difference between the current experiment and a recent crossed-beams experiment[32] is the source of H_2O molecules. A beam of H_2O was formed by allowing pure H_2O vapor, at a stagnation pressure of ∼2.2 Torr, to expand into the scattering chamber through a cluster of capillary tubes. A stainless steel reservoir containing nanopure H_2O was placed in a temperature-controlled water bath, held at −10 °C. The water was degassed in three freeze−pump−thaw cycles. A 1.0-cm-long cluster of ∼60 capillaries (each 0.3 mm OD and ∼0.1 mm ID, with a total cluster diameter of 2.5 mm) was glued with Torr-Seal into the end of a 0.25 in. OD stainless steel tube leading from the H_2O reservoir to the apparatus. The cluster was positioned such that the end of the cluster was 5 mm from the axis of the hyperthermal O-atom beam.

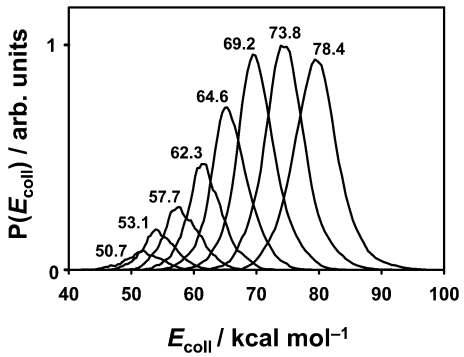

Figure 3. Collision energy distributions for $O(^3P) + H_2O$ collisions. The distributions correspond to eight atomic oxygen beam velocity distributions selected with the use of a synchronized chopper wheel. The average collision energies in kcal mol^{-1} for the respective distributions are shown.

The H_2O beam that exited the cluster crossed the hyperthermal O-atom beam at a nominal angle of 90°. The center of this crossing region contained the axis of rotation of the rotatable mass spectrometer detector. The cross-sectional diameter of the O-atom beam at the crossing region was defined to be ~3.0 mm by a skimmer. The diameter of the H_2O beam at the crossing region was not well defined, but it is assumed that the majority of the intensity of the beam lay within a diameter of 3 mm as a result of the focusing effect of the cluster. Although the H_2O beam was continuous, the hyperthermal O-atom beam was pulsed at a repetition rate of 2 Hz. The pulse width at the crossing region was ~20 μs long [full width at half-maximum (FWHM)], and the flux of O atoms at the crossing region was estimated to be $\sim 3 \times 10^{13}$ atoms cm^{-2} $pulse^{-1}$.[37] The flux of H_2O at the crossing region was not measured, but it might be as high as $\sim 10^{19}$ molecules cm^{-2} s^{-1}, based on the assumption of effusive flow and an inverse-square relationship between flux and distance from the nozzle. Although the H_2O flux was relatively high, there were still relatively few molecules in the crossing region during the O-atom pulse, and multiple collision events in the crossing region were determined from a variety of tests to be negligible.

The H_2O beam was characterized by mounting the chopper wheel in front of the entrance to the detector and aligning the detector with the beam axis. Time-of-flight (TOF) distributions of $m/z = 18$ (H_2O^+) were collected, and other mass-to-charge ratios (e.g., $m/z = 36$, 35) characteristic of dimers or clusters were scanned for signal. No evidence of H_2O dimers or clusters was found. The measured TOF distributions were used to determine the velocity distribution of the H_2O beam. The average velocity was ~800 m s^{-1}, and the velocity range (FWHM) was 550−1000 m s^{-1}.

Time-of-flight distributions of eight O-atom beams, selected with the synchronized chopper wheel, were collected with the detector aligned with the hyperthermal beam axis. From each TOF distribution, a velocity distribution of the hyperthermal O atoms was derived, which, in turn, allowed for the determination of a collision-energy distribution in the c.m. reference frame for $O + H_2O$. The c.m. collision energy distributions corresponding to the eight O-atom beams used in the experiment are shown in Figure 3. Time-of-flight distributions of inelastically and reactively scattered products were collected as a function of flight time from the crossing region of the two beams to the ionizer, which was 33.66 cm away. The relative fluxes of scattered products were derived with the use of the relationship, $\text{flux}(\Theta) \propto \Sigma N(t)/t$, where Θ is the laboratory detector angle with respect to the O-atom beam. For each nominal c.m. collision energy, the detector was placed so that it was aligned with the velocity vector corresponding to the c.m. of the $O + H_2O$ system. The TOF distributions were, thus, collected with a laboratory angle, Θ, that varied from 6° to 7°. Reactively scattered products were detected at $m/z = 33$ (HO_2^+), with integrated count rates from ~0 counts s^{-1} to 1.1×10^5 counts s^{-1}. Inelastically scattered products were detected at $m/z = 16$ (O^+) and 32 (O_2^+), with integrated count rates in the ranges 3.5×10^6 to 8.3×10^6 and 5.8×10^6 to 6.3×10^6 counts s^{-1}, respectively. The $m/z = 32$ TOF distributions were used to correct the $m/z = 16$ TOF distributions for the contribution to the $m/z = 16$ distributions that comes from dissociative ionization of O_2 in the electron-bombardment ionizer. This correction is 11% of the signal detected at $m/z = 32$. Each corrected TOF distribution collected at $m/z = 16$ was integrated with the appropriate velocity weighting, yielding the relative flux. This flux, which is proportional to the flux of the incident O-atom beam, was used to normalize the integrated flux of the HO_2 signal observed with the corresponding collision energy.

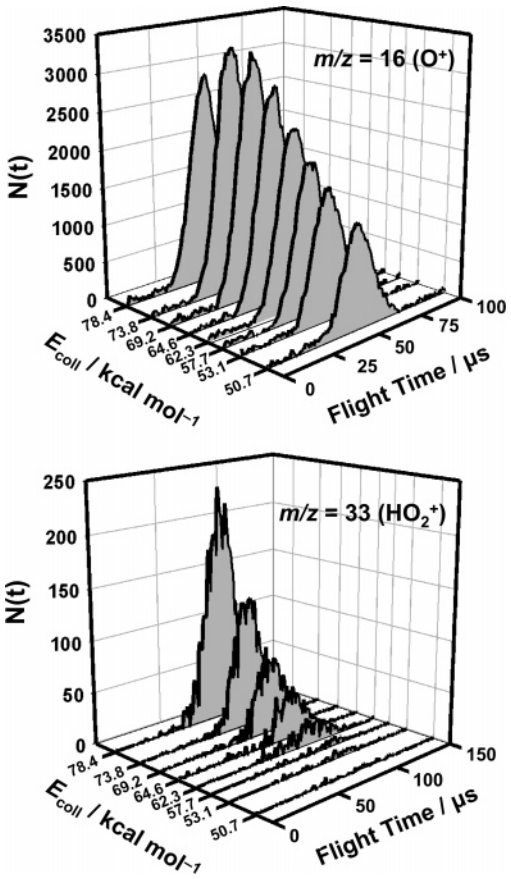

Figure 4. Time-of-flight (TOF) distributions of inelastically scattered O atoms (top) and reactively scattered HO_2 molecules (bottom). Eight TOF distributions were collected for both products corresponding to eight nominal center-of-mass collision energies.

IV. Results and Discussion

Figure 4 shows TOF distributions of inelastically scattered O and reactively scattered HO_2 corresponding to the eight average c.m. collision energies from 50.7 to 78.4 kcal mol^{-1}. The scattered HO_2 flux increases with collision energy, but part of this increase reflects the increasing O-atom flux with the velocity of the hyperthermal beam. The relative flux of inelastically scattered O atoms is taken to be a faithful representation of the relative flux of O atoms in the incident beam pulse, because the inelastic process is not tied to a barrier

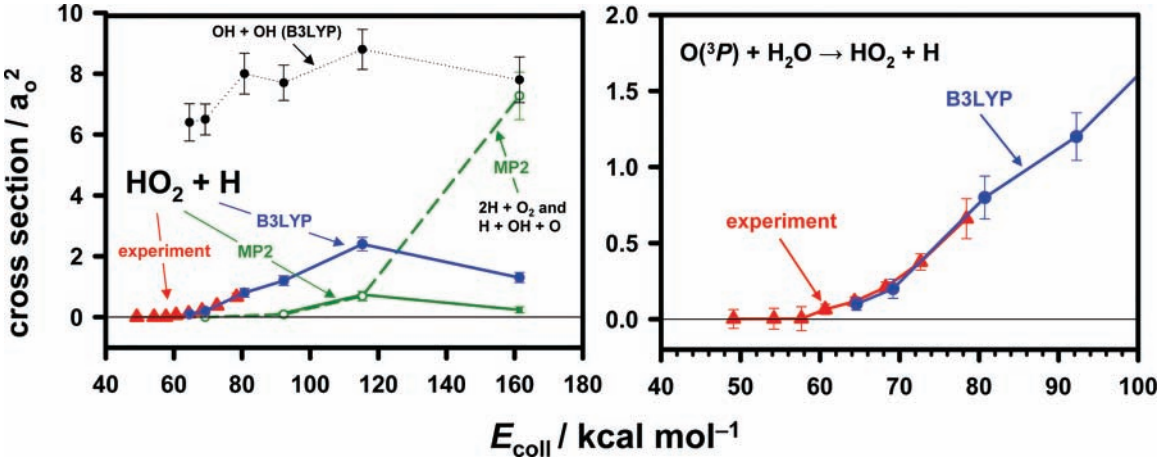

Figure 5. Experimental and theoretical excitation functions for the reaction of $O(^3P)$ with H_2O. A close-up view of the threshold region for the $O(^3P) + H_2O \rightarrow HO_2 + H$ reaction is displayed in the right panel. The solid red triangles are the experimental results for the $HO_2 + H$ product channel, and the solid blue circles are corresponding results from calculations on the B3LYP/6-31G(d,p) surface. The experimental excitation function has been scaled by a constant factor to match the B3LYP function. The solid black squares are the results from calculations on the MP2/6-31G(d,p) surface. The open black circles connected with the dashed line represent the excitation function for production of three products ($2H + O_2$ or $H + OH + O$). The solid black circles connected by a dotted line represent the excitation function for the H-atom abstraction reaction to produce $OH + OH$, calculated with the B3LYP/6-31G(d,p) level of theory.

and the inelastic cross section is therefore not expected to vary significantly over the relatively narrow range of experimental collision energies.[38] Hence, the HO_2 flux was normalized to the flux of inelastically scattered O atoms at the corresponding c.m. collision energy.

The integrated (and normalized) flux of the HO_2 product as a function of c.m. collision energy is shown in Figure 5. The experimental threshold was found to be 60 ± 2 kcal mol^{-1}. The uncertainty in this result is estimated and takes into account both the uncertainty in the integrated flux and the distribution of collision energies at any given nominal beam energy. The observed threshold is slightly higher than the reaction endoergicity of 53.4 kcal mol^{-1}.

The $HO_2 + H$ excitation functions derived from the direct dynamics calculations are also shown in Figure 5. The experimental excitation function was scaled by a constant factor so that its shape could be compared directly to the excitation function calculated at the B3LYP/6-31G(d,p) level of theory. These B3LYP calculations yielded a harmonic zero-point-corrected barrier of 56.2 kcal mol^{-1}, which is very close to the experimentally observed threshold of 60 ± 2 kcal mol^{-1}. The excitation function derived from the MP2/6-31G(d,p) direct dynamics calculations has the same qualitative shape as the B3LYP results, but the threshold is shifted to higher energies. This shift is expected because the barrier to HO_2 formation is $\sim$28 kcal mol^{-1} higher on MP2 than B3LYP. The shape of the experimental and theoretical excitation functions are essentially the same, suggesting that this system can be well described using adiabatic dynamics on the lowest lying (triplet) PES, for the collision energies probed in this work.

The theoretical calculations provide details about the reaction mechanism that go beyond what can be learned from the experimental data. The mechanism is found to be analogous to the reaction mechanism when $O(^3P)$ reacts with HCl to produce ClO.[18] The theoretical excitation function for HO_2 increases up to $\sim$115 kcal mol^{-1} and then begins to decrease as the collision energy increases further. Concomitant with the decrease in the HO_2 excitation function, the excitation function for the production of three products (either $2H + O_2$ or $H + OH + O$) increases sharply. Although it is conceivable that three-product trajectories result from the direct fragmentation of the H_2O product, we do not observe these events in our calculations. Rather at high collision energies, the primary HO_2 products undergo secondary dissociation, and only a fraction of the trajectories lead to stable HO_2. Thus, at these energies fragmentation can be viewed as a multistep process: (1) reaction to form HO_2 followed by (2) unimolecular dissocation of HO_2.

The majority of the trajectories that lead to $HO_2 + H$ at collision energies less than $\sim$110 kcal/mol proceed through an S_N2-like mechanism such as that represented in Figure 6a. In this mechanism, the reagent O atom approaches the O atom in H_2O, and the H atom opposite the incoming O atom is eliminated. These trajectories lead to backward scattering of HO_2. The heavy + heavy−light mass combination and the impulsive transfer of translational energy to the eliminated H atom limits the maximum amount of translational energy of the product pair.[18] Therefore, as the collision energy increases, the internal excitation of HO_2 increases, causing it to dissociate at higher collision energies. The fraction of HO_2 products that dissociate thus increases with increasing collision energy, and the cross section for producing HO_2 decreases. Although this work did not study the partitioning between HO_2 vibration and rotation, one might expect that the H + HL mass combination causes the initial orbital angular momentum **L** to appear as product rotation **J′**. However, examination of the opacity functions for HO_2 formation reveals that small impact parameters are favored and thus **L** and **J′** will be limited.

Collisions in which an H atom is oriented toward the incoming O atom, represented by the trajectory in Figure 6b, tend to transfer more energy into product translation than S_N2-like trajectories similar to that represented in Figure 6a. These trajectories are mainly responsible for the formation of HO_2 at collision energies greater than $\sim$115 kcal/mol and lead to forward and sideways scattering of HO_2. The additional translational energy results from the repulsive force between the incoming O atom and the exiting H atom. Trajectories with the H atom oriented toward the reagent O atom have lower cross sections than S_N2-like trajectories, but they allow sufficient energy in translation that the HO_2 product can be stable even at higher collision energies. As the collision energy increases, the cross section for producing HO_2 begins to decline with the onset of secondary dissociation, and the angular distribution of stable HO_2 shifts from mainly backward to sideways and forward. Figure 7 shows c.m. velocity-flux maps, derived from

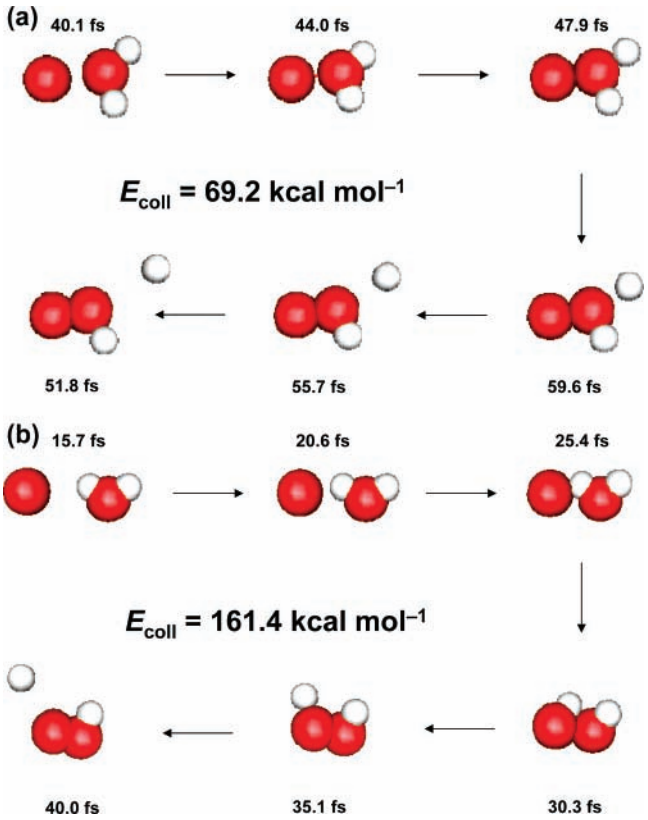

Figure 6. Trajectories for $O(^3P) + H_2O$ collisions, from B3LYP/6-31G(d,p) direct dynamics calculations, with geometries that may lead to $HO_2 + H$, where (a) the HO_2 is scattered in the forward direction with respect to reagent O atom and (b) the HO_2 is scattered in the backward direction. The collision energy in (a) is 69.2 kcal mol^{-1}, and the collision energy in (b) is 161.4 kcal mol^{-1}. At collision energies below ~115 kcal mol^{-1} trajectories resembling (a) dominate the production of HO_2, whereas at collision energies above ~115 kcal mol^{-1} trajectories resembling (b) dominate the production of HO_2 that does not contain enough internal energy to dissociate.

Ⓦ Animated trajectories for Ⓦ Figure 6a and Ⓦ Figure 6b in mpeg format are available on line.

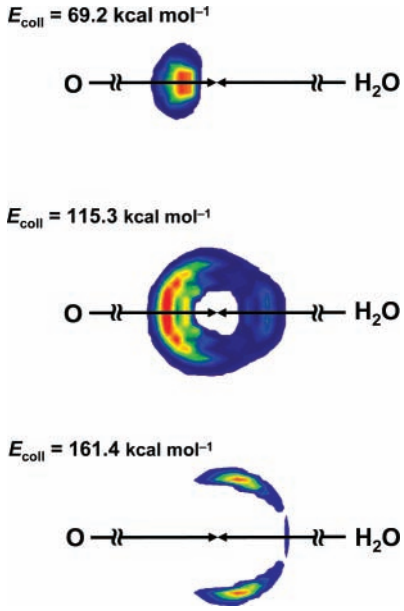

Figure 7. Center-of-mass velocity-flux maps for HO_2, derived from theoretically calculated (B3LYP) translational energy and angular distributions. The results for three collision energies are shown. Each velocity-flux map is normalized such that the red color represents maximum flux. The fraction of HO_2 scattered in the forward direction (with respect to the initial direction of the reagent O atoms) increases with collision energy.

calculated c.m. translational energy and angular distributions, that illustrate the change in the velocity and angular distributions of HO_2 at three collision energies.

The calculated cross sections for the $O(^3P) + H_2O \rightarrow HO_2 + H$ reaction are roughly 10−25% of those for the $O(^3P) + H_2O \rightarrow OH + OH$ reaction in the collision energy range 70−160 kcal mol^{-1} (see Figure 5). In contrast, the H-atom elimination reaction has a comparable cross section to the H-atom abstraction reaction in the analogous $O(^3P) + HCl$ system.[18] In the reactions of $O(^3P)$ with both H_2O and HCl, H-atom abstraction to form OH + OH and OH + Cl proceeds by way of a stripping mechanism (large impact parameters), and the cross sections are similar; thus, the difference in the relative probability of H-atom elimination is not related to the efficiency of abstraction. The significantly larger cross section for the $O(^3P) + HCl \rightarrow ClO + H$ reaction as compared to the $O(^3P) + H_2O \rightarrow HO_2 + H$ reaction can be explained by the relatively large size of the Cl atom, which presents a larger target to the reagent O atom than does the O atom in H_2O.

V. Conclusion

The $O(^3P) + H_2O \rightarrow HO_2 + H$ reaction excitation function was measured in a crossed-beams experiment that employed a source of hyperthermal $O(^3P)$ atoms, and the experimental findings were augmented by direct dynamics calculations. The experimental barrier was found to be 60 ± 2 kcal mol^{-1}, and the shape of the experimental excitation function in the threshold region matched the excitation function calculated at the B3LYP/6-31G(d,p) level of theory for reaction on the lowest triplet potential energy surface. Direct dynamics calculations on this surface showed that the excitation function for production of HO_2 rises from threshold to a maximum near 115 kcal mol^{-1} and then decreases when HO_2 can be formed with sufficient internal energy to dissociate. At collision energies up to ~115 kcal mol^{-1}, an S_N2-like mechanism dominates, and HO_2 scatters mainly in the backward direction with respect to the initial direction of the reagent O atoms. When the collision energy is greater than ~115 kcal mol^{-1}, the only trajectories that lead to stable HO_2 are those in which an H atom is oriented toward the incoming reagent O atom, in which case the HO_2 scatters in the sideways and forward directions. Therefore, the scattering dynamics of HO_2 exhibit a marked dependence on the collision energy, arising from a qualitative change in the reaction mechanism as the energy increases from near-threshold (~60 kcal mol^{-1}) to greater than ~115 kcal mol^{-1}.

Acknowledgment. This work was supported by grants from the Air Force Office of Scientific Research (FA9550-04-1-0428 and FA9550-07-1-0095) and by the Missile Defense Agency under Cooperative Agreement HQ0006-05-2-0001. A.L.B. is grateful for fellowships from the Zonta Foundation and the Montana Space Grant Consortium.

References and Notes

(1) Green, B. D.; Caledonia, G. E.; Wilkerson, T. D. *J. Spacecraft Rockets* **1985**, *22*, 500.

(2) Pickett, J. S.; Murphy, G. B.; Kurth, W. S.; Goertz, C. K.; Shawhan, S. D. *J. Geophys. Res.* **1985**, *90*, 3487.

(3) Wulf, E.; Vonzahn, U. *J. Geophys. Res.* **1986**, *91*, 3270.

(4) Meyerott, R. E.; Swenson, G. R.; Schweitzer, E. L.; Koch, D. G. *J. Geophys. Res.* **1994**, *99*, 17559.

(5) Koch, D. G.; Fazio, G. G.; Hoffman, W.; Melnick, G.; Rieke, G.; Simpson, J.; and Witteborn, F. *Adv. Space Res.* **1987**, *7*, 211.

(6) Dean, D. A.; Huppi, E. R.; Smith, D. R.; Nadile, R. M.; Zhou, D. K. *Geophys. Res. Lett.* **1994**, *21*, 609.

(7) Bernstein, L. S.; Elgin, J. B.; Pike, C. P.; Knecht, D. J.; Murad, E.; Zehnpfennig, T. F.; Galica, G. E.; Stair, A. T. *J. Geophys. Res.* **1996**, *101*, 383.

(8) Caledonia, G. E. Infrared Radiation Produced in Ambient/Spacecraft-Emitted Gas Interactions Under LEO Conditions. *Proceedings of the 38th AIAA Aerospace Sciences Meeting & Exhibit*, held in Reno, NV, 10−13 January 2000; AIAA: Reston, VA, 2000; AIAA-00-0104.

(9) Bernstein, L. S.; Chin, Y. H.; Gardner, J. A.; Broadfoot, A. L.; Lester, M. I.; Tsiouris, M.; Dressler, R. A.; Murad, E. *J. Phys. Chem. A* **2003**, *107*, 10695.

(10) Braunstein, M.; Panfili, R.; Shroll, R.; Bernstein, L. *J. Chem. Phys.* **2005**, *122*, 2736.

(11) Caledonia, G. E.; Krech, R. H.; Oakes, D. B.; Lipson, S. J.; Blumberg, W. A. M. *J. Geophys. Res.* **2000**, *105*, 12833.

(12) Redmon, M. J.; Schatz, G. C. *Chem. Phys.* **1981**, *54*, 365.

(13) Upschulte, B. L.; Oakes, D. B.; Caledonia, G. E. Optical Excitation of Gases in Fast Oxygen Atom Collisions. *IRIS Specialty Group on Targets, Background, and Discrimination*; Hanscom Air Force Base: MA, 1991.

(14) Orient, O. J.; Chutjian, A.; Murad, E. *Phys. Rev. Lett.* **1990**, *65*, 2359.

(15) Karkach, S. P.; Osherov, V. I. *J. Chem. Phys.* **1999**, *110*, 11918.

(16) The direct dynamics calculations in the present work suggest that the reaction $O(^3P) + H_2O \rightarrow H_2 + O_2$ does not occur in hyperthermal collisions of $O(^3P)$ with H_2O. Therefore, this reaction is not discussed further.

(17) Troya, D.; Schatz, G. C.; Garton, D. J.; Brunsvold, A. L.; Minton, T. K. *J. Chem. Phys.* **2004**, *120*, 731.

(18) Camden, J. P.; Schatz, G. C. *J. Phys. Chem. A* **2006**, *110*, 13681.

(19) Arnold, D. W.; Xu, C. S.; Neumark, D. M. *J. Chem. Phys.* **1995**, *102*, 6088.

(20) Deyerl, H. J.; Clements, T. G.; Luong, A. K.; Continetti, R. E. *J. Chem. Phys.* **2001**, *115*, 6931.

(21) Shao, Y.; Molnar, L. F.; Jung, Y.; Kussmann, J.; Ochsenfeld, C.; Brown, S. T.; Gilbert, A. T. B.; Slipchenko, L. V.; Levchenko, S. V.; O'Neill, D. P.; DiStasio, R. A.; Lochan, R. C.; Wang, T.; Beran, G. J. O.; Besley, N. A.; Herbert, J. M.; Lin, C. Y.; Van, Voorhis, T.; Chien, S. H.; Sodt, A.; Steele, R. P.; Rassolov, V. A.; Maslen, P. E.; Korambath, P. P.; Adamson, R. D.; Austin, B.; Baker, J.; Byrd, E. F. C.; Dachsel, H.; Doerksen, R. J.; Dreuw, A.; Dunietz, B. D.; Dutoi, A. D.; Furlani, T. R.; Gwaltney, S. R.; Heyden, A.; Hirata, S.; Hsu, C. P.; Kedziora, G.; Khalliulin, R. Z.; Klunzinger, P.; Lee, A. M.; Lee, M. S.; Liang, W.; Lotan, I.; Nair, N.; Peters, B.; Proynov, E. I.; Pieniazek, P. A.; Rhee, Y. M.; Ritchie, J.; Rosta, E.; Sherrill, C. D.; Simmonett, A. C.; Subotnik, J. E.; Woodcock, H. L.; Zhang, W.; Bell, A. T.; Chakraborty, A. K.; Chipman, D. M.; Keil, F. J.; Warshel, A.; Hehre, W. J.; Schaefer, H. F.; Kong, J.; Krylov, A. I.; Gill, P. M. W.; Head-Gordon, M. *Phys. Chem. Chem. Phys.* **2006**, *8*, 3172.

(22) Werner, H.-J.; Knowles, P. J.; Lindh, R.; Manby, F. R.; Schütz, M.; Celani, P.; Korona, T.; Rauhut, G.; Amos, R. D.; Bernhardsson, A.; Berning, A.; Cooper, D. L.; Deegan, M. J. O.; Dobbyn, A. J.; Eckert, F.; Hampel, C.; Hetzer, G.; Lloyd, A. W.; McNicholas, S. J.; Meyer, W.; Mura, M. E.; Nicklass, A.; Palmieri, P.; Pitzer, R.; Schumann, U.; Stoll, H.; Stone, A. J.; Tarroni, R.; Thorsteinsson, T. MOLPRO, v. 2006.1, a package of *ab initio* programs.

(23) Knowles, P. J.; Hampel, C.; Werner, H. J. *J. Chem. Phys.* **1993**, *99*, 5219.

(24) Johnson, B. G.; Gonzales, C. A.; Gill, P. M. W.; Pople, J. A. *Chem. Phys. Lett.* **1994**, *221*, 100.

(25) Zhao, Y.; Lynch, B. J.; Truhlar, D. G. *J. Phys. Chem. A* **2004**, *108*, 2715.

(26) Pu, J.; Truhlar, D. G. *J. Phys. Chem. A* **2005**, *109*, 773.

(27) Press, W. H.; Flannery, B. P.; Teukolsky, S. A.; Vetterling, W. T. *Numerical Recipes in FORTRAN: The Art of Scientific Computing*, 2nd ed.; Cambridge University Press: Cambridge, England, 1992.

(28) Bunker, D. L. *Proceedings of the International School of Physics Enrico Fermi Course XLIV: Molecular Beam and Reaction Kinetics*; Schlier, C., Ed.; Academic Press: New York, 1970; pp 315−319.

(29) Kumar, S.; Sathyamurthy, N.; Ramaswamy, R. *J. Chem. Phys.* **1995**, *103*, 6021.

(30) Troya, D.; Lakin, M. J.; Schatz, G. C.; González, M. *J. Chem. Phys.* **2001**, *115*, 1828.

(31) Dong, E.; Setser, D. W.; Hase, W. L.; Song, K. *J. Phys. Chem. A* **2006**, *110*, 1484.

(32) Garton, D. J.; Brunsvold, A. L.; Minton, T. K.; Troya, D.; Maiti, B.; Schatz, G. C. *J. Phys. Chem. A* **2006**, *110*, 1327.

(33) Zhang, J. M.; Upadhyaya, H. P.; Brunsvold, A. L.; Minton, T. K. *J. Phys. Chem. B* **2006**, *110*, 12500.

(34) Lee, Y. T.; Mcdonald, J. D.; Lebreton, P. R.; Herschbach, D. R. *Rev. Sci. Instrum.* **1969**, *40*, 1402.

(35) Caledonia, G. E.; Krech, R. H.; Green, B. D. *AIAA J.* **1987**, *25*, 59.

(36) Caledonia, G. E.; Krech, R. H.; Green, B. D.; Pirri, A. N. "Source of High Flux Energetic Atoms," Physical Sciences, Inc., U.S. Patent No. 4,894,511, 1990.

(37) The O-atom flux produced by the hyperthermal source at a distance of 40 cm from the nozzle was determined to be 2×10^{15} atoms cm^{-2} $pulse^{-1}$ by the etch depth of a Kapton H sample (Buczala, D. M.; Brunsvold, A. L.; Minton, T. K. *J. Spacecraft Rockets* **2006**, *43*, 421) after exposure to 100 000 pulses of the hyperthermal O-atom beam. The O-atom flux of the unchopped beam at a distance of 99 cm from the nozzle, where it crossed the H_2O beam, was determined by assuming that the flux decreased from its value at 40 cm by a factor of $(40/99)^2$. The chopper wheel reduces the beam flux by roughly an order of magnitude, although the actual reduction could be more or less than a factor of 10 depending on which part of the beam pulse is selected.

(38) The weak dependence of inelastic cross sections with collision energy is illustrated in: Schatz, G. C. *J. Chem. Phys.* **1980**, *72*, 3929.

(39) Chase, M. W.; Davies, C. A.; Downey, J. R.; Frurip, D. J.; Mcdonald, R. A.; Syverud, A. N., JANAF Thermochemical Tables, Third Edition. *J. Phys. Chem. Ref. Data* **1985**, *14*, Suppl. No. 1.

(40) Ruscic, B.; Wagner, A. F.; Harding, L. B.; Asher, R. L.; Feller, D.; Dixon, D. A.; Peterson, K. A.; Song, Y.; Qian, X. M.; Ng, C. Y.; Liu, J. B.; Chen, W. W. *J. Phys. Chem. A* **2002**, *106*, 2727.

(41) Sayos, R.; Oliva, C.; Gonzalez, M. *J. Chem. Phys.* **2001**, *115*, 8828.

(42) Ruscic, B.; Pinzon, R. E.; Morton, M. L.; Srinivasan, N. K.; Su, M. C.; Sutherland, J. W.; Michael, J. V. *J. Phys. Chem. A* **2006**, *110*, 6592.